JOURNAL OF MATERIALS SCIENCE 20 (1985) 612–619

Observation of dislocations and subboundaries in the optically active crystal $Bi_{12}GeO_{20}$ with reflection birefringence topography

XIU-YING XU, DUAN FENG
Department of Physics and Institute of Solid State Physics, Nanking University, Nanking, China

The birefringence topography of a $Bi_{12}GeO_{20}$ single crystal which has a strong natural optical activity is presented. The natural optical activity of the crystal may be completely compensated by reflection polarised light microscopy so that the birefringence images of dislocations and subboundaries are observed. The Burgers' vectors of dislocations were found to be of the types 1/2 ⟨111⟩, ⟨100⟩ and ⟨110⟩ and dislocations which form subboundaries are also of these types.

1. Introduction

Birefringence topography has been proved to be an effective method for the investigation of defects in transparent crystals. Birefringence images of dislocations and other defects in crystals have been studied both experimentally and theoretically [1–12]. However, previous studies were limited to the transmission method which is unsuitable for crystals with strong optical activity. Using a reflection method, we have successfully observed the birefringence images of dislocations in the optically active crystal $Bi_{12}GeO_{20}$. The initial results have been briefly reported in a Chinese journal [13]. In this paper we give a more detailed report.

2. Theoretical basis

Bullough [2] developed a mathematical description of the intensity contour around an edge dislocation if viewed end on between crossed polarizers. It implicitly assumes that the crystal is initially strain-free. A more realistic approach to the calculation of the intensity distribution must take into account the inevitable presence of a long-range strain in the crystal. Tanner and Fathers [8] calculated the intensity of a long-range plane strain superposed on the strain fields of dislocations and the result may be expressed in the following formula:

$$I = U_0 \sin 2(\phi - \alpha) - \frac{2\mathbf{b}U_0 \sin 2(\phi - \alpha) \cos\psi \cos 2(\psi - \alpha)}{\pi r} - \frac{\mathbf{b}^2 \cos^2\psi \cos 2(\psi - \alpha)}{(\pi r)^2} \quad (1)$$

where U_0 is the magnitude of the principal strain of the long-range strain fields, α the angle between the dislocation slip plane (or X-axis) and the analyser direction, ϕ the angle between the direction of principal strain of the long-range fields and Burgers' vector $\mathbf{b}$. In this formula the first and third terms are the intensities caused by the plane strain field and the strain field of dislocation respectively, the second is an interaction term.

There are three special cases:

1. $\alpha = 0$, $0 < \phi \leqslant 45°$

the intensity contour is shown in Fig. 1a. When U_0 is negative, a six-petal rosette is shown with alternate dark and bright regions. When U_0 is positive, the intensity is reversed.

2. $\alpha = 45°$, $\phi = 45°$

as shown in Fig. 1c, all petals in the four-petal rosette are bright.

0022–2461/85 $03.00 + .12

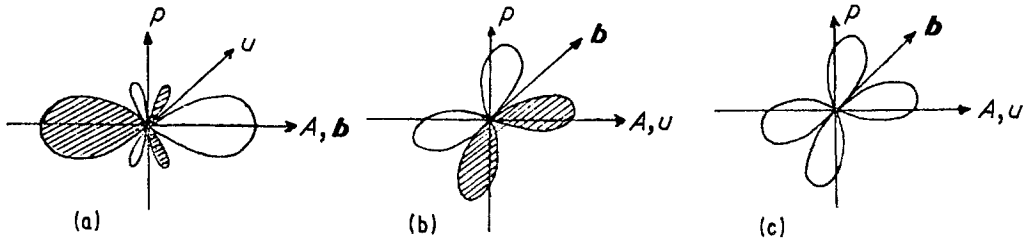

Figure 1 The intensity contour of a dislocation viewed end on: (a) $\alpha = 0°$, $0 < \phi \leqslant 45°$; (b) $\alpha = 45°$, $0 < \phi < 45°$; (c) $\alpha = 45°$, $\phi = 45°$.

3. $\alpha = 45°$, $0 < \phi < 45°$

as shown in Fig. 1b, two petals in the four-petal rosette are bright and two dark. A is the direction of the analyser, P is the direction of the polarizer. It is seen from this discussion that the Burgers' vector can be easily determined from these special cases of the birefringence topography, after the crystal orientation has been determined by X-ray methods.

3. Experimental procedure

BGO ($Bi_{12}GeO_{20}$) crystals belong to the cubic system with space group I23, and the lattice constant, $a = 1.01455$ nm [14]. Since BGO is strongly optically active, we can not observe the birefringence images of dislocations with transmission microscopy due to the effect of chromatic dispersion. However, the natural optical activity of the crystal may be compensated completely in reflection microscopy with polarized light [14]. In a natural optically active crystal the angle of rotation of the polarization plane is proportional to $(\omega L/2c)$ (g/n_0), where L is the path length traversed by the light, ω the circular frequency, c the velocity of light in a vacuum, n_0 the index of refraction and g the coefficient of optical activity.

The sign of g is determined by the chirality of the crystal structure and is independent of the direction of light. When light traverses the same path twice as in the reflection method, the rotation of the polarization plane cancels out completely [15].

The schematic diagram for reflection microscopy used is shown in Fig. 2. We used a Leitz Orthoplan polarizing microscope in the reflection mode to observe the birefringence images of dislocation in BGO crystal.

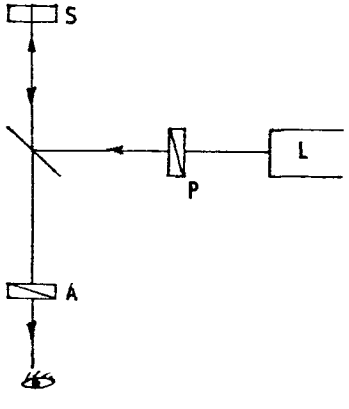

Figure 2 The schematic diagram for reflection microscopy: S = specimen; P = polarizer; A = analyser; L = lamp.

4. Sample preparation

BGO single crystals were grown by the Czochralski method [16]. The growth axes of the crystal are mostly along ⟨1 0 0⟩, ⟨1 1 0⟩ and ⟨1 1 1⟩ with deviations about several degrees. Crystal wafers suitable for observation were prepared by the usual methods of cutting, grinding and polishing. Wafers 1 to 2 mm thick were mostly used. Since BGO crystals are quite soft, we used the powder of Alumina 305# in grinding, followed by polishing with diamond grinding grease from 2 to 0.5 μm.

5. Results

5. 1. Straight dislocations viewed end on

Birefringence images of dislocations obtained when transverse sections of as-grown crystals are observed with crossed polars are shown in Fig. 3.

(a) $\alpha = 0$: The six-petal rosette consists of alternate dark and bright petals.

(b) $\alpha = 45°$: The four-petal rosette consists of two dark and two bright petals.

(c) $\alpha = 45°$; $\phi = 45°$: The four-petal rosette consists of four bright petals and the background is dark, showing that the long-range strain fields around dislocations disappear.

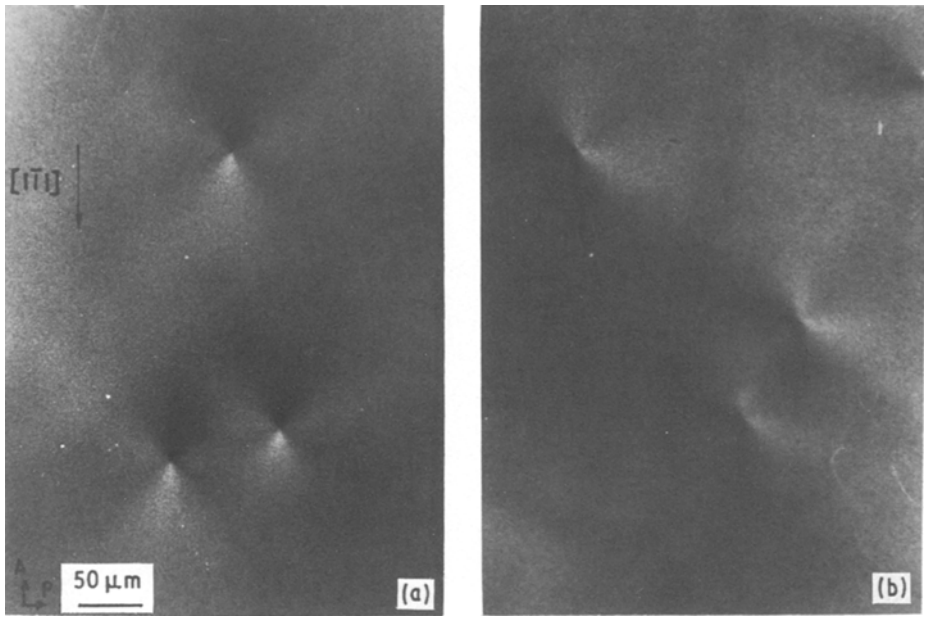

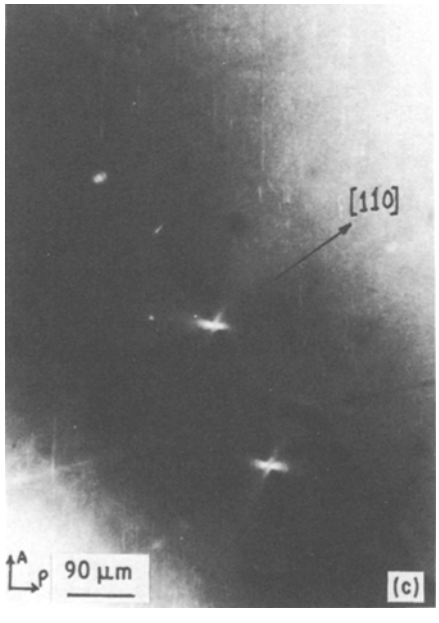

Figure 3 Birefringence images of individual edge dislocation viewed end on: (a) $\alpha = 0$, observation plane is (1 1 0); (b) $\alpha = 45°$, observation plane is (1 1 0); (c) $\alpha = 45°$, $\phi = 45°$, observation plane is (0 0 1).

These results agree with those of the theoretical calculation by Tanner and Fathers [8]. The images of four bright petals ($\alpha = 45°$, $\phi = 45°$) were rarely observed in the experiments. This is to be expected since the condition for the appearance of the four bright petals is very critical. The angle between **b** (Burgers' vector), A and U (the direction of analyser and the principal strain of long-range field) must be equal to 45° simultaneously. The direction of the principal strain then coincides with that of analyser or polarizer.

Burgers' vectors of straight dislocations along different growth axes were determined for a number of specimens and the results are shown in Table I. The types of dislocations may be estimated from the edge components of the Burgers' vectors since the screw components make no contribution to the birefringence images of dislocations viewed end on. Straight edge dislocations were found to be the types 1/2 ⟨1 1 1⟩, ⟨1 0 0⟩ and ⟨1 1 0⟩. This conforms with the theoretical expectations of bcc crystals. In the (1 1 1) plane the edge dislocation along ⟨1 2 1⟩ with Burgers' vector **b** = 1/2 ⟨1 1 1⟩ and mixed dislocations have been observed more frequently.

When the dislocation lies with a large angle to the normal of the observed surface, the images of dislocation lines appear as lines as shown in Fig. 4. For the dislocations along $[\bar{1}\,2\,\bar{1}]$ and $[1\,1\,\bar{2}]$ the angle between which equals 60° when rotating the specimen, it is found that the image will never vanish. According to the extinction rules as formulated by Tanner and Fathers [8], it can be verified that they are composed of mixed dislocations with the Burgers' vectors [0 1 0] and $1/2\,[1\,1\,\bar{1}]$.

5. 2. Subboundaries

For dislocations with the same sign forming

TABLE I Types of dislocations determined with birefringence topography

Observation plane	(001)			(110)		(111)	
Direction of dislocation	[001]			[110]		[111]	[121]
Slip plane	(010)	$(\bar{1}10)$	$(\bar{1}10)$	(001)	$(\bar{1}12)$	$(2\bar{1}\bar{1})$	$(10\bar{1})$
Burgers' vector	[100]	[110] $\frac{1}{2}$ [$\bar{1}\bar{1}$1]	[001] $\frac{1}{2}$ [111] $\frac{1}{2}$ [11$\bar{1}$]	[$\bar{1}$10] [100]	[010] $\frac{1}{2}$ [1$\bar{1}$1]	[0$\bar{1}$1] $\frac{1}{2}$	[111]
Type of dislocation	90°	90° 54°	90° 35°	90° 45°	90°	90°	90°

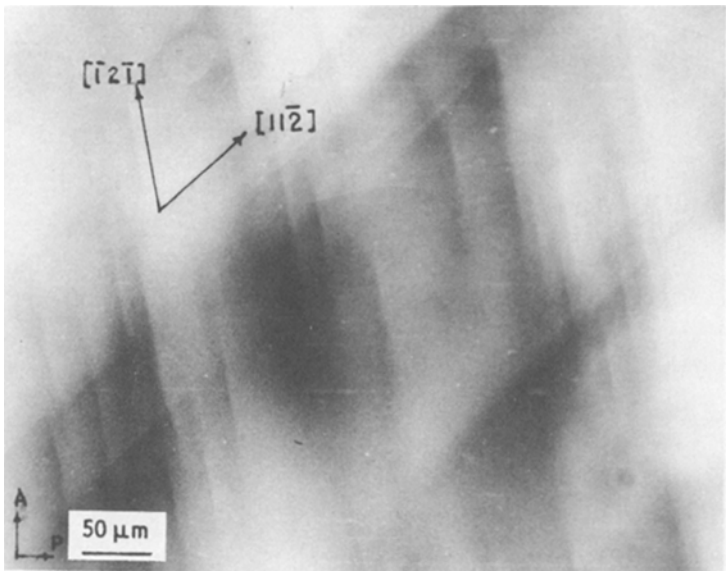

Figure 4 The birefringence images of inclined dislocation lines in (111).

symmetric tilt subboundaries, commonly observed with birefringence topography, we can determine parameters of subboundaries such as the direction of the subboundary, the type of dislocations which composed the subboundary and the relationship between the subboundary and strain fields. A row of dislocations with the same Burgers' vector [001] which lines up along [110] is shown in Fig. 5, the images of individual dislocations can still be distinguished. By changing the focus of the microscope we can observe the subboundary running through the whole specimen from the upper surface to the lower one nearly perpendicular to the crystal surface. This is a symmetric tilt boundary with the boundary normal along [001]. On the other hand the distance between dislocations can be measured from the micrograph and so the tilt angle of the subboundary is found to be $\theta = 5.8 \times 10^{-3}$ degrees.

It should be noted that the black–white con-

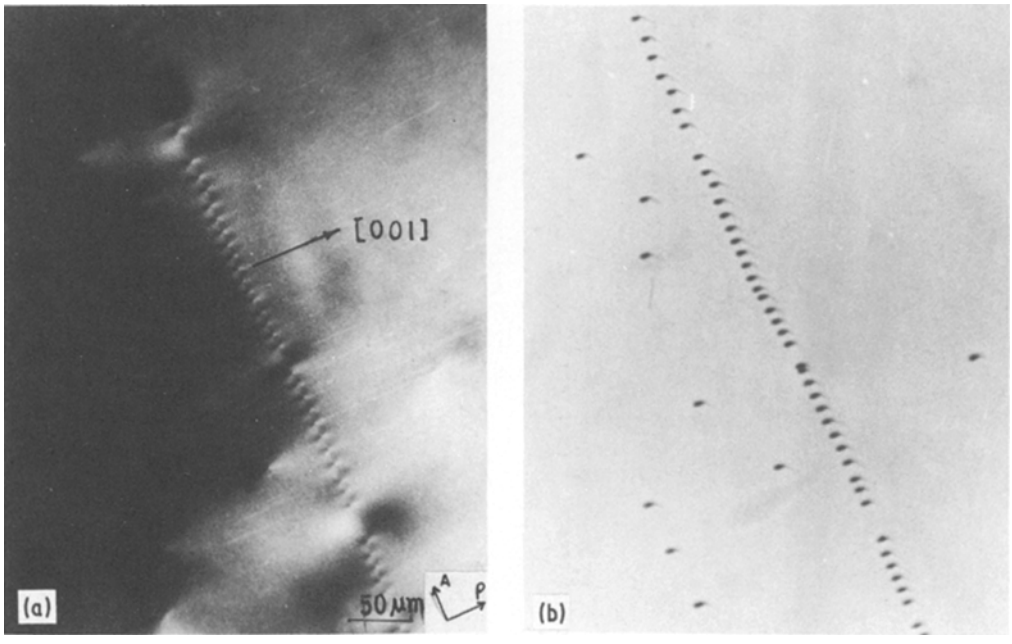

Figure 5 Subboundary composed of dislocations **b** = [001] [observation plane is (110)]: (a) birefringence image; (b) the etch pattern of the same.

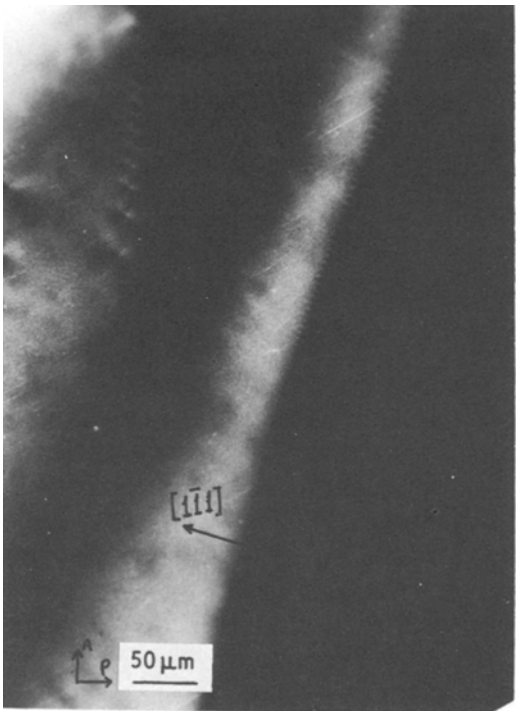

Figure 6 Subboundary composed of dislocations with $\mathbf{b} = \frac{1}{2}[1\,\bar{1}\,1]$ [observation plane is (1 1 0)].

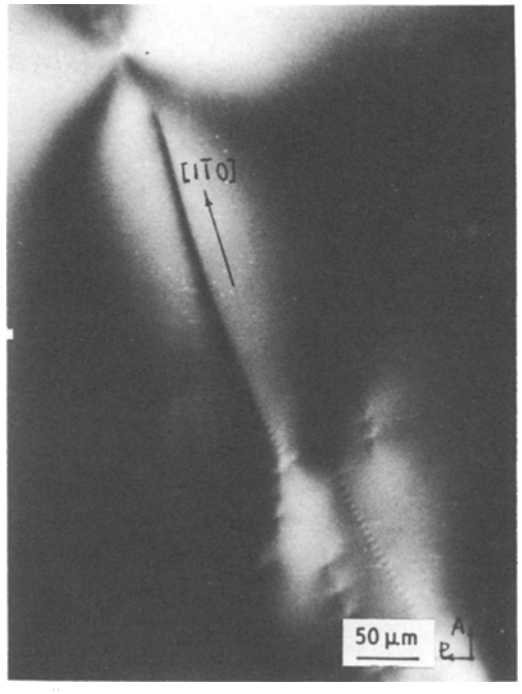

Figure 7 Subboundary composed of dislocations with $\mathbf{b} = \frac{1}{2}[1\,1\,\bar{1}]$ [observation plane is (1 1 1)].

trast was very irregular along the subboundary due to the inhomogeneous strain field, which probably also caused the nonuniform arrangement of dislocations.

Fig. 5b shows the etch-pattern of the same area indicating that there is a one to one correspondence between etch-pits and birefringence images of dislocations.

In Fig. 6, a subboundary composed of $\mathbf{b} = 1/2\,[1\,\bar{1}\,1]$ dislocations is seen on the right and a wall terminating within the crystal on the left. It may be seen that near the terminus the dislocation spacing increases, causing a change in size of the strain pattern of the dislocation indicating that this part of the boundary becomes non-ideal.

In Fig. 7 we show a subboundary composed of dislocations with a Burgers' vector $\mathbf{b} = 1/2\,[1\,1\,\bar{1}]$ which inclines about 7° to the normal of the observation surface (it further deviates about 7° to the (1 1 1) plane). The subboundaries and its parameters deduced from observations are shown in Table II.

Experimental evidence shows that subboundaries are composed of dislocations with Burgers' vectors 1/2 ⟨1 1 1⟩, ⟨0 0 1⟩ or ⟨1 1 0⟩ in BGO crystals and the **b** vector coincides with the normal vector **n** of the subboundaries. These are stable subboundaries. Sometimes metastable subboundaries may be observed with the **b** vector deviating from the normal vector **n** or containing dislocations

TABLE II Subboundaries and their parameters deduced by observations with birefringence topography

Observation plane	(0 0 1)		(1 1 0)		(1 1 1)
Direction of dislocation line	[0 0 1]		[1 1 0]		[1 1 2]
Burgers' Vector	[1 0 0]	[1 $\bar{1}$ 0]	[0 0 1]	$\frac{1}{2}$ [1 $\bar{1}$ 1]	$\frac{1}{2}$ [1 1 $\bar{1}$]
Direction of trace of subboundary	[0 $\bar{1}$ 0]	[$\bar{1}$ $\bar{1}$ 0]	[1 $\bar{1}$ 0]	[$\bar{1}$ 1 2]	[1 1 0]
Normal vector of subboundary	[1 0 0]	[1 $\bar{1}$ 0]	[0 0 1]	[1 $\bar{1}$ 1]	[1 1 $\bar{1}$]
Distance between dislocations (µm)	20	30	10	5–10	6–2
Tilt angle	5.1×10^{-3}	4.8×10^{-3}	5.8×10^{-3}	$10 \times 10^{-2} - 5 \times 10^{-2}$	$8.4 \times 10^{-3} - 2.5 \times 10^{-2}$

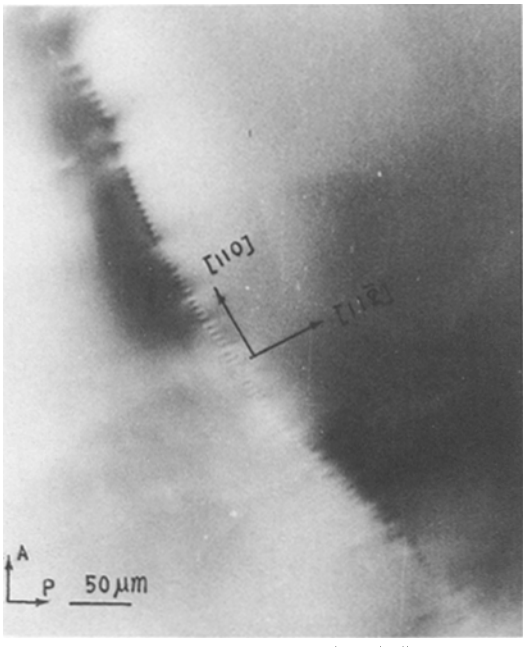

Figure 8 Metastable subboundary composed of dislocations with $\mathbf{b} = \frac{1}{2}[1\,1\,\bar{1}]$ showing the nonuniform arrangement [observation plane is (1 1 1)].

with a nonuniform arrangement as shown in Fig. 8 and Fig. 9a. After annealing these metastable subboundaries may be transformed into more stable ones (see Fig. 9b). Fig. 9a shows a subboundary which is composed of $\mathbf{b} = [001]$ dislocations. It is to be noted that both when the **b** vector deviates from the normal vector **n** and when the arrangement of dislocations with $\mathbf{b} = 1/2[1\,\bar{1}\,\bar{1}]$ is nonuniform due to an inhomogeneous long-range strain around them, these subboundaries are metastable. After annealing at 700° C for 7 h it is found that there is a change of the long-range strain field, and the subboundary becomes divided into two parts. The spacing between dislocations decreases, and the orientations turn to nearly that of the symmetric tilt boundary (see Fig. 9b).

5.3. Dislocations with strain pattern of larger than normal size

Sometimes dislocations with strain patterns of larger than normal size have been observed and these mostly occur in crystals with rather degraded optical quality. Some of these presumably may be due to the overlapping of the strain pattern of close, parallel, neighbouring dislocations (see Fig. 10). Such dislocation bundles have a large effective Burgers' vector.

Others are dislocations decorated by small precipitates (see Fig. 11). It is found that the visibility of dislocations in birefringence topography may be enhanced through decoration of very fine precipitates [17].

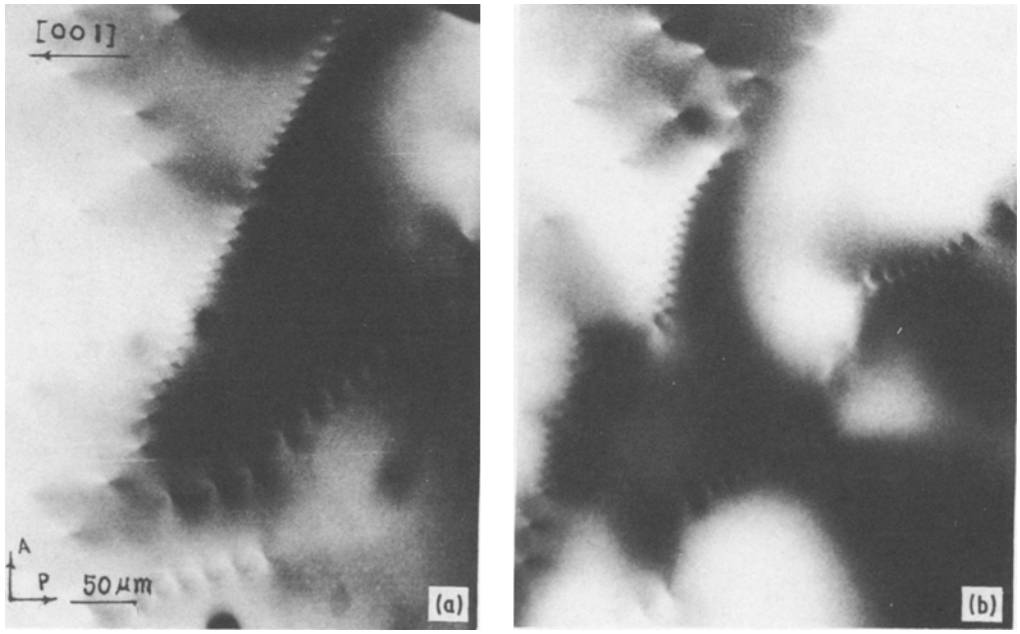

Figure 9 The effect of annealing on two rows of dislocations composed of Burgers' vectors $\mathbf{b} = \frac{1}{2}[111]$ and [001] respectively: (a) before annealing the **b** vector was deviated from the normal vector **n**; (b) after annealing at 700° C for 7 h the normal of subboundaries line up parallel to the Burgers' vectors.

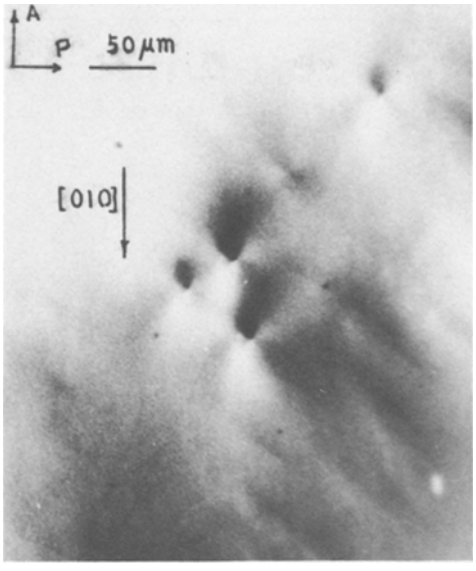

Figure 10 The overlapping of strain patterns of neighbouring dislocations.

Acknowledgements

The authors are indebted to Mr Xin-chu Wang and Mr Bang-chun Shi for their help and the supply of a number of BGO specimens. The authors would like also to express gratitude to Miss Jing-li Diao and Mr Shan-lin Ni for assistance with experimental work. This work is supported by Science Funds of Chinese Academy of Sciences.

References

1. W. L. BOND and J. ANDRUS, *Phys Rev.* **101** (1956) 1211.
2. R. BULLOUGH, *ibid.* **110** (1958) 620.
3. V. L. INDENBOM, V. I. NIKITENKO and L. S. MILEVSKI, *Sov. Phys. Sol. Stat.* **4** (1962) 162.
4. D. A. JENKINS and J. J. HREN, *Phil. Mag.* **33** (1976) 173.
5. J. W. MATTHEWS, E. KLOKHOLM, V. SADAGOPAN, T. S. PLASKETT and E. MENDEL, *Acta Metall.* **21** (1973) 203.
6. D. J. FATHERS and B. K. TANNER, *Phil. Mag.* **27** (1973) 17.
7. *Idem, ibid.* **28** (1973) 749.
8. B. K. TANNER and D. J. FATHERS, *ibid.* **29** (1974) 1081.
9. J. W. MATTHEWS, T. S. PLASKETT and S. E. BLUM, *Crystal Growth* **42** (1977) 621.
10. H. S. BAGDASAROV and L. M. DODUK, *Kristallogr.* **15** (1970) 334.
11. J. W. MATTHEWS and T. S. PLASKETT, *Phil. Mag.* **33** (1976) 73.
12. S. Y. SHU (X. Y. XU), Z. Z. KUO (C. Z. GE) and D. FONG (D. FENG), *J. Phys.* **C6** (1980) 186.
13. S. Y. SHU (X. Y. XU) and D. FONG (D. FENG), *Acta Phys. Sin.* **29** (1980) 1636.
14. S. C. ABRAHAMS, P. B. JAMIESON and J. L. BERNSTEIN, *J. Chem. Phys.* **47** (1967) 4035.
15. L. D. LANDAU and E. M. LIFSHITZ, "Electrodynamics of Continuous Media", (Pergamon Press, Oxford, 1960) p. 337.
16. Z-G. HU, G. LU and X-C. WANG, *Piezoelectrics and Acoustooptics* **3** (1979) 12.
17. B. K. TANNER, *Phil. Mag.* **49** (1984) 435.

Received 13 March
and accepted 6 April 1984

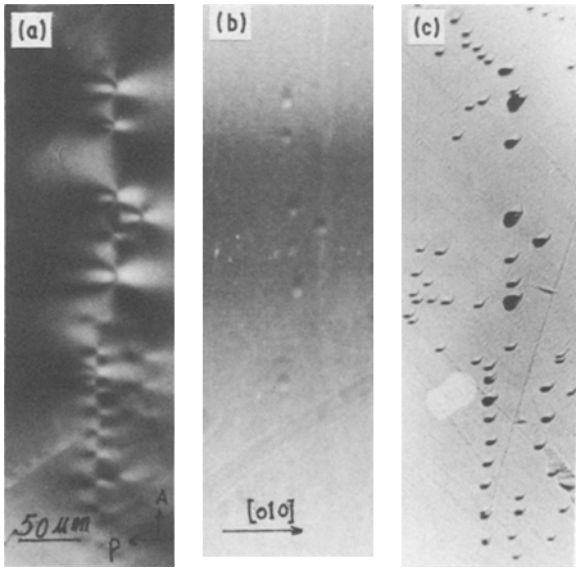

Figure 11 Decorated dislocations: (a) birefringence images; (b) decorated particles seen by ordinary transmission microscopy; (c) etch-pits of dislocation of the same area.